



Fabrication of n-type CuInS₂ modified TiO₂ nanotube arrays heterostructure photoelectrode with enhanced photoelectrocatalytic properties

Tingting Li^{a,b}, Xinyong Li^{a,c,*}, Qidong Zhao^a, Yong Shi^a, Wei Teng^a

^a Key Laboratory of Industrial Ecology and Environmental Engineering, School of Environmental Sciences and Technology, Dalian University of Technology, Dalian 116024, China

^b College of Civil Engineering and Architecture, Liaoning Technical University, Fuxin 123000, China

^c Department of Chemical Engineering, University of Cape Town, Cape Town 7701 Rondebosch, South Africa

ARTICLE INFO

Article history:

Received 11 November 2013

Received in revised form 17 March 2014

Accepted 19 March 2014

Available online 27 March 2014

Keywords:

Photoelectrocatalytic

n-Type

CuInS₂

2-Chlorophenol

ABSTRACT

A novel n-type CuInS₂ modified TiO₂ nanotube arrays (NTs) heterostructure photoelectrode was successfully prepared via an ultrasonication-assisted cathodic electrodeposition strategy. CuInS₂ particles were uniformly decorated on the inner and external walls of the TiO₂ NTs electrode. The stoichiometry measured by XPS and ICP-OES clearly illustrated the excess indium. Mott–Schottky analysis further demonstrated CuInS₂ possessed an n-type feature. Optical characterizations indicated that the introduced CuInS₂ could extend the visible-light response range and enhance the visible light photoactivity. Moreover, the electrochemical measurements attested to a significant improvement of the interfacial electron-transfer properties. The photoelectrocatalytic (PEC) activity of CuInS₂/TiO₂ NTs electrode was evaluated by degradation of 2-chlorophenol (2-CP) under visible light irradiation ($\lambda > 420$ nm). The results indicated that the as-prepared CuInS₂/TiO₂ NTs electrode displayed much higher PEC performance than that of the pure TiO₂ NTs electrode.

© 2014 Elsevier B.V. All rights reserved.

1. Introduction

Ever since Zwilling et al. synthesized TiO₂ NTs by anodization in HF containing electrolyte [1], this highly ordered one dimensional (1D) architecture has attracted tremendous scientific and technological interest in water splitting [2–4], dye-sensitized solar cell [5–8], gas sensors [9–12], degradation of hazardous wastes [13–16], owing to the outstanding properties, high physical and chemical stability, biocompatibility and efficiency of harvesting incident photons.

However, because of the wide band gap (3.0 eV for rutile phase and 3.2 eV for anatase phase), TiO₂ could only be excited by UV light, which limits the effective utilization of solar light [17]. Besides, low quantum efficiency and the recombination between the photo-generated electrons and holes are also two major factors impeding the enhancement of the photocatalytic activity [18]. In order to

overcome the above limitations, several methods could be adopted to improve the visible light utilization efficiency and the photocatalytic properties, including non-metal doping [19], metal ions doping [20,21], semiconductor modifying [22,23], and precious metal particles loading [24,25].

Modifying TiO₂ NTs with narrow band gap semiconductor is one of the effective methods facilitating the photo-induced charges separation between the foreign semiconductor and TiO₂. To date, considerable experimental efforts have been made to decorate TiO₂ NTs with narrow band gap semiconductors, such as quantum dots of CdS, CdSe and PbS, etc. [26–29]. Nevertheless, in view of the environmental harmfulness of those toxic heavy metals, the green materials are preferred. CuInS₂ has various advantages in photovoltaic applications with a narrow band gap of 1.5 eV, such as high visible-light absorption coefficient [30], good optical stability [31] and low toxicity [32]. Moreover, its conduction band edge is more negative than that of TiO₂, CuInS₂ modified TiO₂ NTs could potentially enhance the charge separation. Many literatures have reported the formation of p–n heterojunction CuInS₂/TiO₂ catalyst with excess copper [33–36]. The decoration of p-type CuInS₂ onto TiO₂ could form a heterojunction structure, which would remarkably facilitate the charge separation, interfacial transfers and visible

* Corresponding author at: Dalian University of Technology, School of Environmental Science & Technology, No. 2, Linggong Road, Dalian, Liaoning 116024, China. Tel.: +86 411 8470 7733; fax: +86 411 8470 7733.

E-mail address: xinyongli@hotmail.com (X. Li).

light utilization. On the other hand, n-type CuInS_2 also has excellent photoelectrochemical conversion efficiency and chemical stability [37,38]. By successfully combining TiO_2 NTs and n-type CuInS_2 nanoparticles to yield a novel n–n heterostructure, the more efficient utilization of the visible light and much improvement of the surface-interface charge transfer could be expected. However, to date, few literatures have reported n-type CuInS_2 due to the difficulty in the control of the excess indium. The control of the excess indium to form n-type CuInS_2 loading on TiO_2 NTs electrode still remains a challenge.

Herein, a novel n-type CuInS_2 modified TiO_2 NTs electrode with n–n heterojunction has been synthesized using a facile ultrasonication-assisted cathodic electrodeposition strategy. Based on a series of systematic characterization, $\text{CuInS}_2/\text{TiO}_2$ NTs electrode exhibited a significant visible-light activity, which could be attributed to the high visible absorption coefficient of CuInS_2 and the formed n–n heterojunction. Furthermore, the efficient PEC degradation of 2-CP under visible light irradiation with the $\text{CuInS}_2/\text{TiO}_2$ NTs electrode was carefully integrated and clarified in terms of the co-relationship between the novel structure of the composite electrode and its remarkable performance.

2. Experimental

2.1. Materials

Ti sheets (0.5 mm thick, 99.7% purity, Beijing Academy of Steel Service, China) were cut into samples of size 20 mm \times 40 mm. All the chemicals were of analytical grade and used as received without further purification. Doubly distilled deionized water was used for the preparation of all solutions and the rinse of Ti sheets.

2.2. Preparation of TiO_2 nanotube arrays on Ti substrate

The highly ordered TiO_2 nanotube arrays were prepared by anodization in a two-electrode electrochemical cell. Before anodization, the Ti foils were first polished with different abrasive papers, and chemically etched in a mixture acid for 40 s, which was prepared by mixing hydrofluoric acid, nitric acid and deionized water (1:4:5 in volume). These foils were rinsed in an ultrasonic bath of ethanol and deionized water for 15 min, respectively, and then dried in nitrogen stream. Anodization was conducted in 0.2 wt% HF aqueous electrolyte with a platinum electrode served as the cathode. A potential of 20 V was kept for 30 min at room temperature. TiO_2 nanotube arrays were subsequently annealed at 500 $^\circ\text{C}$ for 1 h with heating and cooling rate of 2 $^\circ\text{C min}^{-1}$.

2.3. Preparation of CuInS_2 -loaded TiO_2 nanotube arrays

CuInS_2 nanoparticles were deposited onto the TiO_2 NTs by using an ultrasonication-assisted electrodeposition method. A typical three-electrochemical cell was equipped with a platinum electrode as a counter electrode, saturated calomel electrode (SCE) as a reference, and the TiO_2 NTs as the working electrode. Prior to electrodeposition, the TiO_2 NTs was first immersed in a solution containing 0.02 M indium chloride tetrahydrate ($\text{InCl}_3 \cdot 4\text{H}_2\text{O}$), and then immersed in a 0.01 M copper chloride dihydrate ($\text{CuCl}_2 \cdot 2\text{H}_2\text{O}$) solution. Both of the impregnations were under ultrasonication for 5 min with 100 watt power and 80 kHz frequency in a digitally-controlled ultrasonic cleaner (Shumei KQ3200DB). In this process, the ultrasonication plays a role like a capillary action to help the metal ions to diffuse through the nanochannels of TiO_2 [45]. Then, the TiO_2 NTs was put in the typical three-electrochemical cell containing 0.1 M sodium thiosulfate pentahydrate ($\text{Na}_2\text{S}_2\text{O}_3 \cdot 5\text{H}_2\text{O}$)

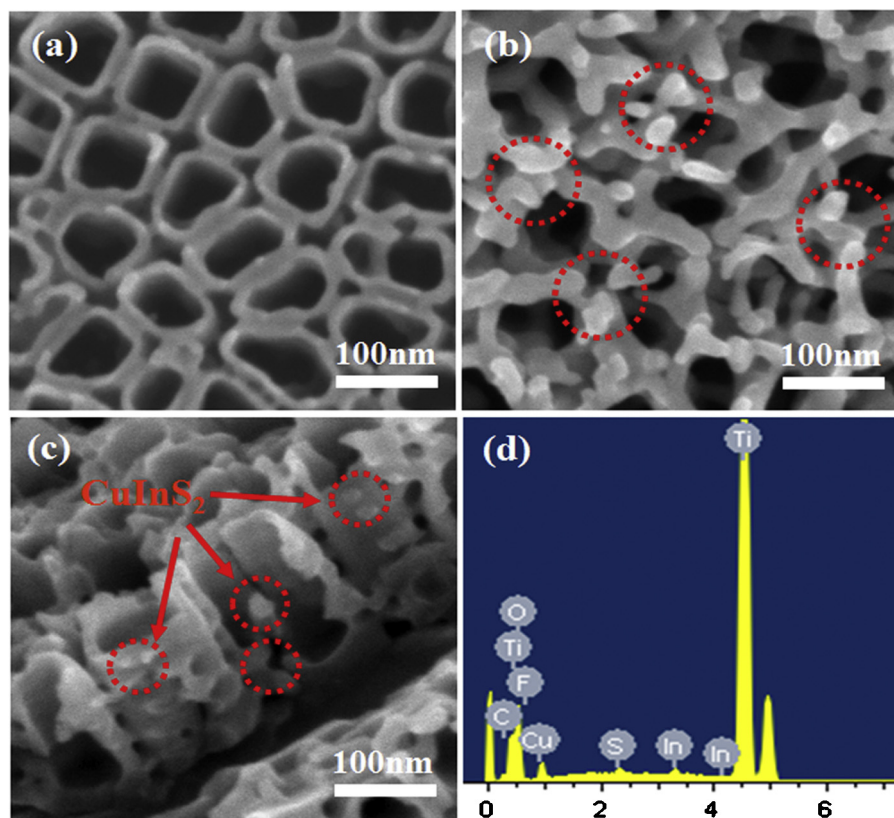


Fig. 1. FESEM image: (a) top-view of TiO_2 NTs, (b) top-view image of $\text{CuInS}_2/\text{TiO}_2$ NTs, (c) cross section of $\text{CuInS}_2/\text{TiO}_2$ NTs and (d) EDX of the as-prepared $\text{CuInS}_2/\text{TiO}_2$ NTs with the experimental parameters as follows: deposition time = 5 min, deposition voltage = -0.9 V, deposition cycles = 10 repetitions, concentration = 0.02 M In and 0.01 M Cu, 0.1 M S, dose of LiCl = 5 mL.

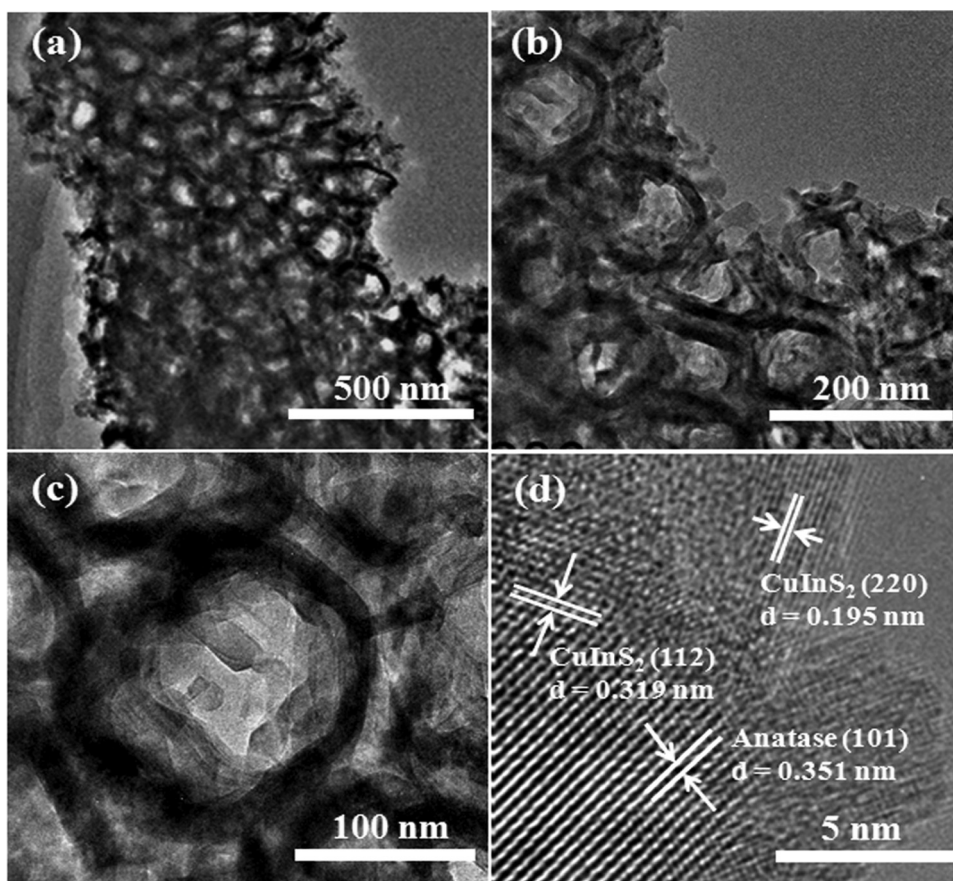


Fig. 2. Low-magnification TEM images (a–c) and high-resolution TEM image (d) of $\text{CuInS}_2/\text{TiO}_2$ NTs.

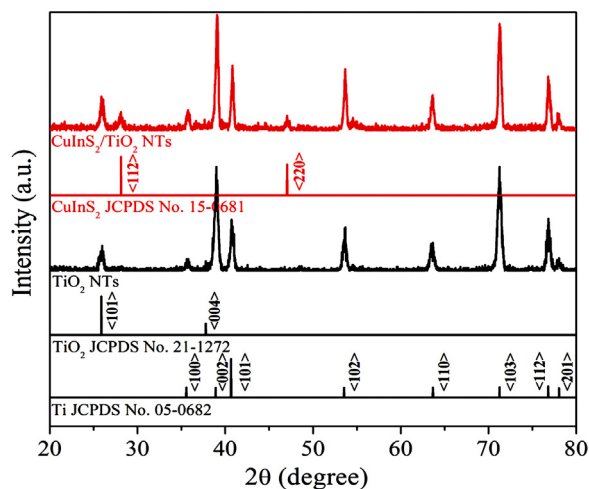


Fig. 3. XRD patterns of TiO_2 NTs and $\text{CuInS}_2/\text{TiO}_2$ NTs.

with 0.20 M lithium chloride (LiCl) as a complexant. The pH was adjusted to 2.5–3.0 by hydrochloric acid. After 10 repetitions of the ultrasonification and electrodeposition, the modified TiO_2 NTs was washed several times and calcined in a nitrogen atmosphere at 350°C for 1 h with heating/cooling rate of 1°C min^{-1} .

2.4. Characterization

The microstructural and morphological features of the samples were characterized by using a field-emission scanning electron

microscopy (Nova NanoSEM 450, USA). The atomic ratio was measured with energy dispersive X-ray (EDX, X-Max OXFORD Instruments). Transmission electron microscopy (TEM) analyses were carried out under a JEOL-2010 electron microscope, using a 200 kV accelerating voltage. The crystalline phases were identified by X-ray diffractometer with $\text{Cu K}\alpha$ irradiation at 30 kV and 30 mA (Lab-XRD-6000, Japan). The compositions of the samples were analyzed by X-ray Photoelectron Spectroscopy (ESCA Lab 250, U.K.). The binding energies were normalized by referencing C 1s (284.6 eV) peak. Inductively coupled plasma-optical emission spectrometry (ICP-OES) was performed to determine the actual Cu/In ratio of the sample on a Perkin-Elmer Optima 3300DV apparatus. UV–vis diffuse reflection spectroscopy (DRS) was carried out on an UV–vis spectrophotometer (JASCO, UV-550, Japan) with a wavelength range of 200–800 nm. The surface photovoltage (SPV) spectroscopy measurement was carried out with a monochromator (Omni- λ 3005) and a lock-in amplifier (SR830-DSP) synchronized with an optical chopper (SR540) at 20 Hz. All experiments were carried out at room temperature (approximately $22\text{--}25^\circ\text{C}$). The photoluminescence (PL) spectra were recorded using a fluorescence spectrophotometer of model Hitachi F94500 with an UV irradiation ($\lambda = 325\text{ nm}$) as the light source.

Electrochemical measurement was performed on a CHI electrochemical analyzer (CHI instruments 760C, China) in a standard three-electrode electrochemical cell, with the $\text{CuInS}_2/\text{TiO}_2$ NTs serving as the work electrode, Pt foil as the counter electrode, and a saturated calomel electrode (SCE) as the reference electrode. The effective area of the electrode is 4 cm^2 in $0.01\text{ M Na}_2\text{SO}_4$. A 500 W xenon lamp with a composited cutoff filter served a wavelength range of 420–800 nm and the measured intensity at the position of illuminated sample was 35.5 mW cm^{-2} .

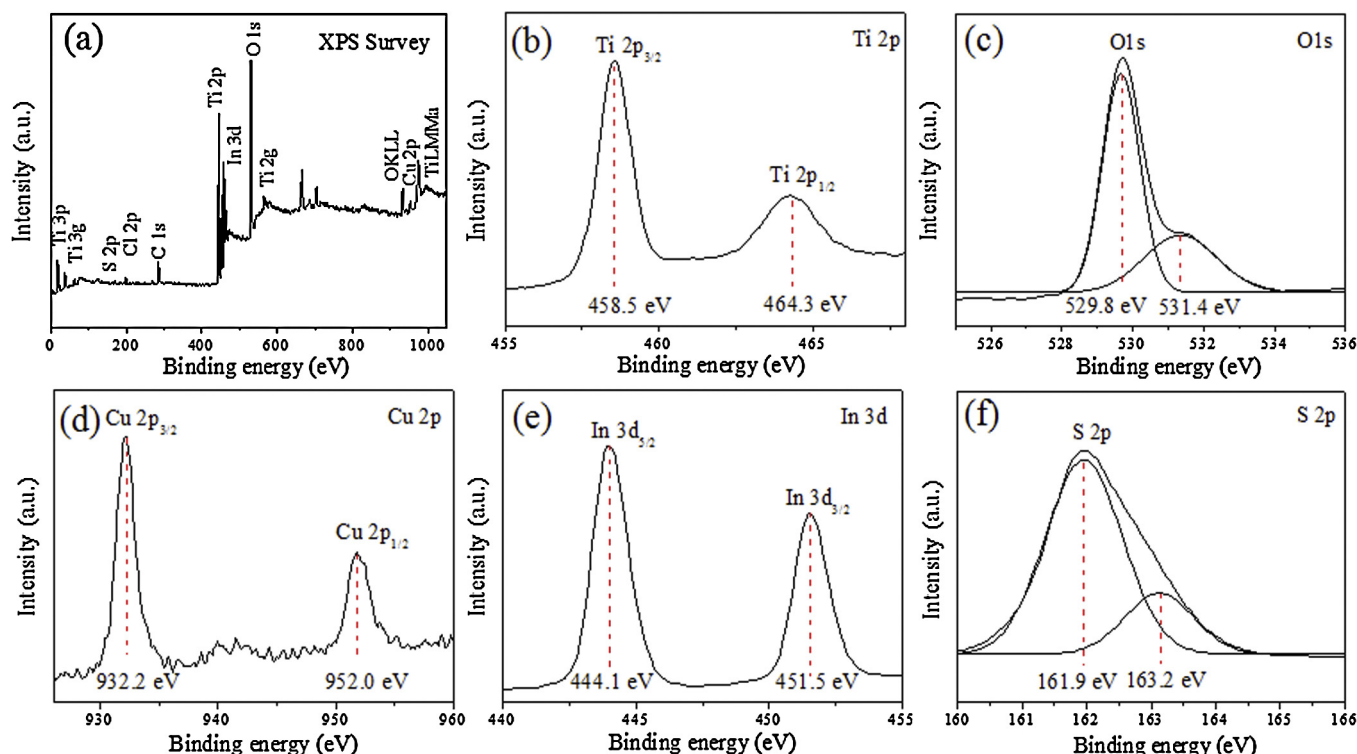


Fig. 4. XPS survey spectrum (a) and high-resolution XPS spectra of Ti 2p (b), O 1s (c), Cu 2p (d), In 3d (e), S 2p (f) for $\text{CuInS}_2/\text{TiO}_2$ NTs.

2.5. Photoelectrochemical measurement

The PEC degradation of 2-CP was carried out in a single photoelectrochemical compartment. Briefly, a quartz reactor was filled with 100 mL of 2-CP (initial concentration: 20 mg L^{-1}) which contained 0.01 M sodium sulfate (Na_2SO_4) at ambient temperature. The visible light source was provided by a 500 W xenon lamp with a composited cutoff filter providing a spectral range of 420–800 nm (35.5 mW cm^{-2}). Photocatalytic degradation was monitored by measuring the absorbance of solution using a UV1100 spectrophotometer and the concentration of 2-CP was determined at its characteristic absorption wavelength of 275 nm. Meanwhile, the same conditions are applied for the total organic carbon (TOC) measurement. Every experiment was repeated for three times to ensure the reliability.

3. Results and discussion

The surface morphologies of the prepared samples depend on the experimental conditions such as deposition cycles, electrochemical times, deposition voltage and concentration of LiCl. Scanning electron microscope (SEM) images for the as-prepared $\text{CuInS}_2/\text{TiO}_2$ NTs electrodes under different electrodeposition conditions are displayed in Fig. S1–4. More detailed information has been provided in the Supporting Information. Fig. 1a shows a typical SEM image of the TiO_2 NTs with an average nanotube diameter of about 100 nm and the wall thickness of about 20 nm. Fig. 1b and c show the top view and side view SEM images of TiO_2 NTs after CuInS_2 modification. It is observed that CuInS_2 nanoparticles with a size of about 25 nm are deposited successfully not only on the external walls but also on the inner walls of the TiO_2 NTs. Apparently, no obvious aggregation of CuInS_2 nanoparticles is observed at the entrance of TiO_2 nanotubes, and the tube diameter becomes relatively narrow due to the deposition. Meanwhile, the well-ordered TiO_2 NTs structure still exists, which means that the electrodeposition process did not destroy the nanotube structure. This is a

prerequisite for fast electron transfer across the NTs on the electrode. The corresponding EDX curve is shown in Fig. 1d, which confirms that Ti, O, In, S, Cu, C and F elements were detected with the specimen. The F and C peaks shown in the EDX spectrum are attributed to the hydrofluoric acid containing electrolyte and the FESEM platform used to support the samples, respectively. The EDX analysis results showed that the atomic ratio of In and S is approximately 1:2. Apparently, the Cu peak is higher than those of In and S. The Cu peaks could be derived from not only the loaded CuInS_2 but also the supporting Cu grid [39].

To further investigate the microstructure characteristics of CuInS_2 nanoparticles deposited on TiO_2 NTs, TEM images of the composite electrode are displayed in Fig. 2. As illustrated by the low magnification TEM images in Fig. 2a–c, CuInS_2 nanoparticles were deposited on the inner and external tubes with the size in the range of 20–30 nm. Additionally, the well-resolved lattice features were identified by high resolution TEM (HRTEM) analyses (Fig. 2d). The lattice fringes of 0.195, 0.319 and 0.351 nm are clearly observed, corresponding to the d-spacing values of the (220), (112) planes of roquesite phase of CuInS_2 (JCPDS 47-1371) and the (101) planes of crystalline anatase (JCPDS 21-1272).

The wide-angle XRD patterns of the TiO_2 NTs and $\text{CuInS}_2/\text{TiO}_2$ NTs are displayed in Fig. 3. The peak at 2θ value of 25.5° and 37.8° corresponds to the (101) and (004) facets of anatase phase of TiO_2 (JCPDS No. 211272) and the peaks at about 2θ values of 35.5° , 38.8° , 40.7° , 53.4° , 63.4° , 71.0° , 76.6° correspond to the (100), (002), (101), (102), (110), (103) and (112) facets of Ti metal (JCPDS No. 050682). Furthermore, the peaks at 2θ values of 28.2° , 47.0° can be well indexed to (112), (220) crystal planes of roquesite phase of CuInS_2 (JCPDS No. 150681). The XRD results suggest that the composite electrode prepared via the ultrasonication-assisted electrodeposition method has well crystalline structure of CuInS_2 and TiO_2 .

To better confirm the states of elements and composition information of the nanotubular samples, XPS characterization was carried out and the results are shown in Fig. 4. It is found that

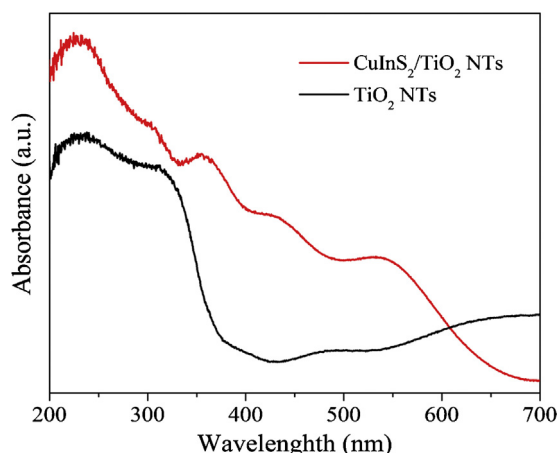


Fig. 5. UV-vis absorption spectra of the as-prepared TiO₂ NTs and CuInS₂/TiO₂ NTs.

the CuInS₂/TiO₂ NTs is mainly composed of Ti, O, C, Cu, In, S and Cl elements. The XPS peak for C 1s at 284.6 eV is used as the internal reference for correcting the binding energy. The Cl element could be derived from the raw materials of InCl₃·4H₂O and CuCl₂·2H₂O. A typical high-resolution spectrum of Ti 2p is shown in Fig. 4b. Two peaks at 464.3 and 458.5 eV are assigned to Ti2p_{1/2} and Ti2p_{3/2}, which is characteristic of Ti⁴⁺ in anatase TiO₂ [40,41]. The XPS spectrum of O 1s can be deconvoluted into two peaks by Gaussian–Lorentzian peak shapes due to its asymmetry in Fig. 4c. The large peak at 529.8 eV is attributed to the lattice oxygen, whereas the lower peak at 531.4 eV is attributed to the surface adsorbed oxygen (hydroxyl group and chemisorbed oxygen-containing species) [42]. The binding energies of the Ti 2p_{3/2} and O 1s match exactly the values of those in TiO₂. Fig. 4d–f show the Cu 2p, In 3d, and S 2p core levels investigated with high-resolution spectra for the valence state and atomic ratio, respectively. The binding energy of Cu2p_{1/2} and Cu2p_{3/2} located at 952.0 and 932.2 eV is corresponding to chemical element state of Cu⁺ [43]. The peaks of binding energy at 444.1 and 451.5 eV match well with 3d electron of In³⁺. Moreover, the S 2p is not a symmetric peak due to the overlapping of Cu–S (161.9 eV) and In–S (163.2 eV) responses, which are separated by an energy difference of 1.3 eV that is consistent with that of CuInS₂ [43]. The above characterization results by SEM, TEM, EDX, XRD and XPS could unanimously reveal that the nanoparticles successfully loaded on the highly ordered TiO₂ NTs can be assigned as CuInS₂. Furthermore, XPS analysis indicates the composition of the electrode is CuIn_{1.12}S_{2.08}. In addition, the Cu/In ratio measured by ICP-OES is 1:1.27. The excess of indium element reveals that CuInS₂ particles fabricated using the facile ultrasonication-assisted electrodeposition strategy could be inferred as an n-type semiconductor.

The UV-vis DRS results of TiO₂ NTs and CuInS₂/TiO₂ NTs electrodes are shown in Fig. 5. TiO₂ NTs electrode exhibits absorption below 390 nm corresponding to the absorption edge ($E_g = 3.2$ eV). Compared with the pure TiO₂ NTs, the CuInS₂ modified electrode demonstrates an absorption spectrum in the entire visible range with a remarkable red shift on the absorbance edge. The widened light absorption spectrum can be attributed to loading CuInS₂, which could absorb the visible light effectively and enhance the visible-light response of the nanotubular composite electrode.

To further demonstrate the behavior of CuInS₂ modification in expanding the active spectral range of TiO₂ to visible light region, the SPV spectra of the as-grown electrodes are measured and the results are shown in Fig. 6. TiO₂ NTs electrode presents a strong response in the UV range from 300 to 380 nm, due to the electron transition from valence band to conduction band of TiO₂ (O_{2p}–Ti_{3d}) [44,45]. CuInS₂/TiO₂ NTs electrode displays a stronger SPV

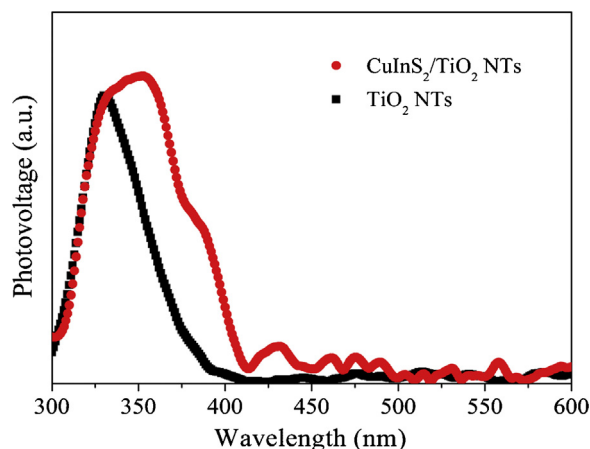


Fig. 6. SPV spectra of the as-prepared TiO₂ NTs and CuInS₂/TiO₂ NTs.

signal than that of TiO₂ NTs electrode. In addition, the modified electrode exhibits a red shift of the spectral band. In view that the strong SPV signal has direct correlation with effective separation of photo-generated charge carriers [46], the present of CuInS₂ would greatly favor the photo-induced charge carrier separation and surface-interface transfers followed by tremendously increasing the photocatalytic and photoelectrocatalytic activity of TiO₂ NTs electrode.

When the recombination of the photo-induced electron–hole pairs occurs, a certain amount of chemical energy can be released, which would further transform possibly to energy forms of heat or luminescence emission by semiconductor material [47]. Thus PL phenomenon occurs consequently. PL spectroscopy is therefore employed to investigate the effect of CuInS₂ modification on the electron–hole recombination behavior of TiO₂ NTs electrode. Fig. 7 presents the PL spectra of TiO₂ NTs and CuInS₂/TiO₂ NTs electrodes under UV excitation at 325 nm. Clearly, TiO₂ NTs electrode shows two strong emission peaks around 390 and 465 nm. The former peak at 390 nm is normally attributed to the free excitons at the band edge of TiO₂ [47], while the other peak at 465 nm is attributed to the oxygen vacancies with energy levels below conduction band [48]. The PL intensity of CuInS₂/TiO₂ NTs electrode is evidently weakened compared to TiO₂ NTs. In general, PL phenomena could be yielded through the band–band PL process and excitonic PL process. For the band–band PL process, the weaker the PL spectrum, the higher the separation rate of photo-induced charge carriers and the higher the photocatalytic activity [47,49,50]. However, the relationship between the excitonic PL intensity and photocatalytic activity is mainly dependent on specific species. Since the

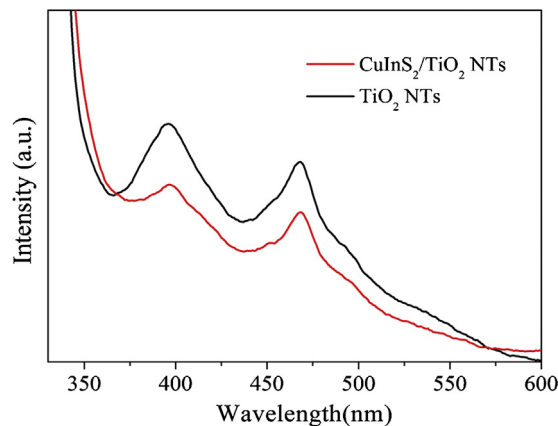


Fig. 7. PL spectra of the as-prepared TiO₂ NTs and CuInS₂/TiO₂ NTs.

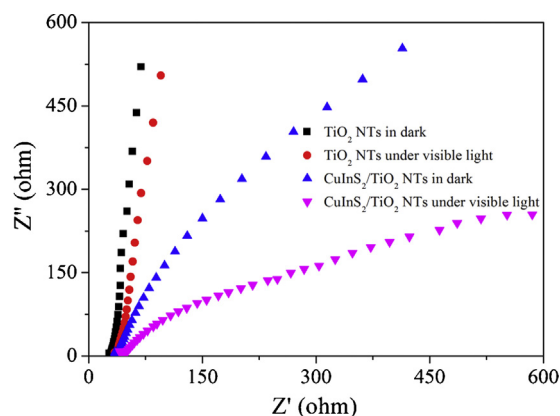


Fig. 8. EIS Nyquist plots of TiO_2 NTs and $\text{CuInS}_2/\text{TiO}_2$ NTs in dark and under visible light irradiation, the bias potential is 0.3 V (vs. SCE) in 0.01 M Na_2SO_4 aqueous solution ($\lambda > 420$ nm, $I = 35.5 \text{ mW cm}^{-2}$).

conduction band edge of CuInS_2 has a higher energy level than TiO_2 [36], it is more favorable for the electrons excited in the conduction band of CuInS_2 to transfer into the conduction band of TiO_2 . Thus, it might be speculated that the weaker the excitonic PL spectrum is, the higher the separation rate of photo-induced electrons and holes is, and potentially the higher the photocatalytic activity as well.

The electrochemical impedance spectrum (EIS) has been demonstrated as a powerful method for studying the charge transfer and recombination processes at semiconductor/electrolyte interfaces in the photocatalytic and photoelectrocatalytic process on TiO_2 electrodes [51]. The EIS Nyquist plots of TiO_2 and $\text{CuInS}_2/\text{TiO}_2$ electrodes were measured in aqueous 0.01 M Na_2SO_4 solution in dark and under visible light irradiation ($\lambda > 420$ nm) (Fig. 8). The frequency is 10^5 – 10^{-2} Hz interval using the amplitude of 5 mV at open-circuit potential. It can be seen clearly from Fig. 8 that the EIS of TiO_2 NTs is almost a straight line, which is due to the fact that pure TiO_2 NTs do not respond to visible light. On the contrary, the curve radius of $\text{CuInS}_2/\text{TiO}_2$ NTs is significantly smaller than that of TiO_2 NTs either in dark or under visible light irradiations. This result confirms that the $\text{CuInS}_2/\text{TiO}_2$ NTs could greatly and effectively improve the separation of photo-generated electron–hole pairs by the anodic bias potential, leading to a fast interfacial charge transfer over $\text{CuInS}_2/\text{TiO}_2$ nanotubular electrodes [52].

To further confirm the type of semiconductor and evaluate the electron-transfer properties of semiconductor interface, Mott–Schottky plots of the potential range (–1.0 to 1.0 V) are provided in dark and under visible light for the as-prepared nanotubular electrodes (Fig. 9). It can be seen from the figure that all the slopes of the curves are positive. As we all know, TiO_2 is n-type semiconductor, which is in good agreement with the positive slope. Likewise, the similar positive slope measured for the $\text{CuInS}_2/\text{TiO}_2$ NTs sample, indicates that the yielded CuInS_2 component is an n-type semiconductor [38,53]. The result of an n-type CuInS_2 is also in good agreement with the XPS and ICP-OES results of excess In element.

The interfacial capacitance C is related to the change carrier density following the equation [54].

$$\frac{1}{C^2} = \frac{2}{\epsilon_0 \epsilon_{\text{TiO}_2} \epsilon_0 N_D} \left[E - E_{\text{FB}} - \frac{kT}{e_0} \right] \quad (1)$$

where ϵ_0 being the permittivity of free space, ϵ_{TiO_2} the permittivity of the semiconductor electrode, e_0 the elementary electron charge, N_D the charge carrier density, E the applied potential, E_{FB} the flatband potential, k the Boltzmann's Constant, T the

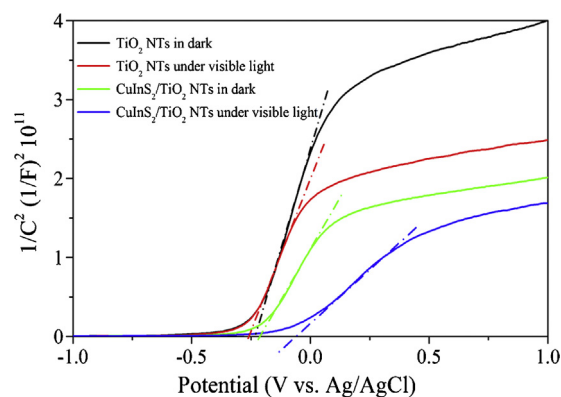


Fig. 9. Mott–Schottky plots measured at a frequency of 10 Hz of TiO_2 NTs and $\text{CuInS}_2/\text{TiO}_2$ NTs in dark and under visible light irradiation, the bias potential is 0.3 V (vs. SCE) in 0.01 M Na_2SO_4 aqueous solution ($\lambda > 420$ nm, $I = 35.5 \text{ mW cm}^{-2}$).

temperature of operation, and the space charge capacitance $C = -1/(2\pi fZ'')$ in case of series capacitance.

According to Eq. (1), the slope of $1/C^2$ vs. potential plot gives the charge carrier density N_D , can be presented in the following equation [55]:

$$N_D = -\frac{2}{e_0 \epsilon_{\text{TiO}_2} \epsilon_0 m} \quad (2)$$

where m is the slope of the Mott–Schottky plot. This equation means that the smaller the slope of the Mott–Schottky curve is, the higher the charge carrier density will be. Apparently, $\text{CuInS}_2/\text{TiO}_2$ NTs electrode under visible light irradiation demonstrates the highest charge carrier density at the semiconductor interface.

To evaluate the photoelectrochemical behaviors of the as-prepared $\text{CuInS}_2/\text{TiO}_2$ electrodes, the photocurrent density vs. applied voltage scans were performed with and without simulated sunlight irradiation (Fig. 10). Apparently, the photocurrent densities of pristine TiO_2 NTs and $\text{CuInS}_2/\text{TiO}_2$ NTs are negligible. The saturated value of TiO_2 NTs electrode is 2.840 mA cm^{-2} at 1.0 V (vs. SCE). Upon the same applied voltage, $\text{CuInS}_2/\text{TiO}_2$ NTs electrode exhibits a stronger photocurrent density, which increases to 5.375 mA cm^{-2} and is roughly 1.9 times as high as the value of the former. An enhanced photoelectrochemical performance of $\text{CuInS}_2/\text{TiO}_2$ electrode was evidenced.

As characterized by means of DRS above, $\text{CuInS}_2/\text{TiO}_2$ demonstrated significant visible light response. The photocurrent densities of as-prepared TiO_2 and $\text{CuInS}_2/\text{TiO}_2$ NTs electrodes under

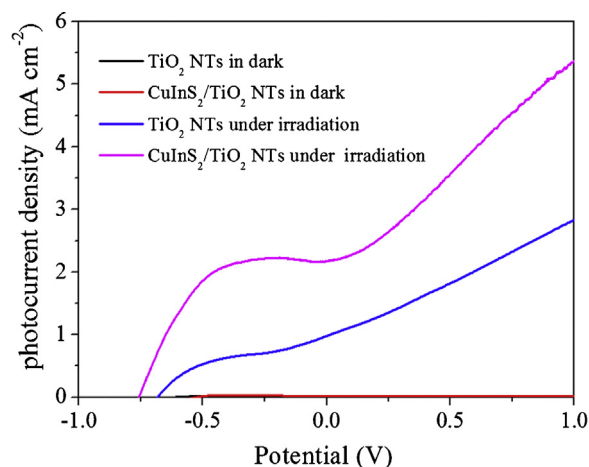


Fig. 10. Photocurrent density vs. bias potential of TiO_2 NTs and $\text{CuInS}_2/\text{TiO}_2$ NTs in dark and under simulated sunlight irradiation ($I = 35.5 \text{ mW cm}^{-2}$).

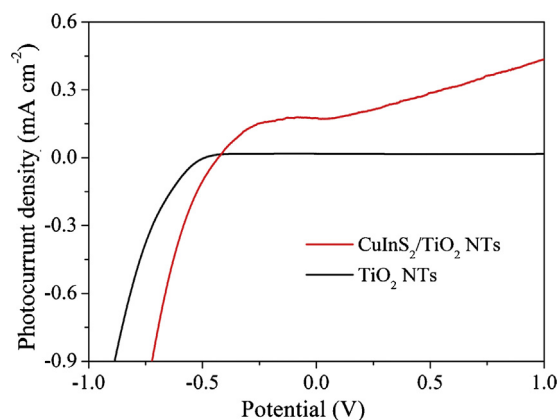


Fig. 11. Photocurrent density vs. bias potential of TiO₂ NTs and CuInS₂/TiO₂ NTs under visible light irradiation ($\lambda > 420$ nm, $I_0 = 35.5$ mW cm⁻²).

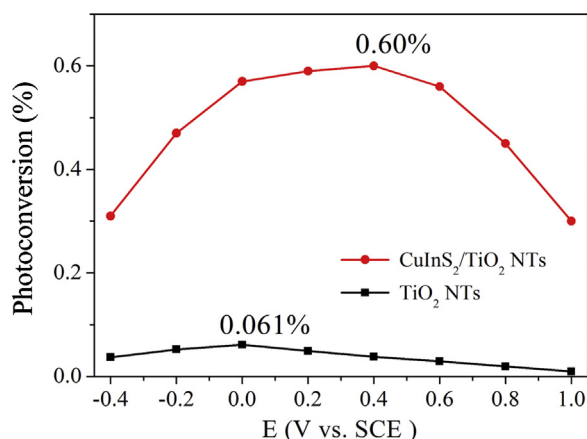


Fig. 12. Photoconversion efficiency of TiO₂ NTs and CuInS₂/TiO₂ NTs under visible light irradiation as a function of applied potential (vs. SCE) under visible light irradiation ($I = 35.5$ mW cm⁻²).

visible light irradiation are further examined and shown in Fig. 11. In the presence of visible light irradiation, the pure TiO₂ NTs electrode is almost flat with zero current under the range from -1.0 to 1.0 V. While upon the same illumination, the photocurrent density of the CuInS₂/TiO₂ electrode increases markedly to about 0.436 mA cm⁻², which is 26.1 times as high as the value of the pure TiO₂ NTs electrode (0.0167 mA cm⁻²) under the bias potential below 1.0 V. The significant enhancement in photocurrent response under the visible light ($\lambda > 420$ nm) depends on the strong visible absorbance of CuInS₂ as well as the reduction of recombination between photo-generated electrons and holes by the formed n-n heterojunction between CuInS₂ species and titania nanotubes.

Fig. 12 shows the total photoconversion efficiency over the applied voltage of the as-prepared samples. The photoconversion efficiency is calculated using the following equation [33,56],

$$\eta(\%) = \frac{\text{total power output} - \text{electrical power input}}{\text{light power input}} \times 100$$

$$= [j_p(E_{\text{rev}}^0 - |E_{\text{app}}|) \times 100] / I_0 \quad (3)$$

In this equation, j_p is the photocurrent density (mA cm⁻²), E_{rev}^0 the standard state-reversible potential, which is 1.23 V vs. NHE, and I_0 is the intensity of incident light (mW cm⁻²), and the applied potential is $E_{\text{app}} = E_{\text{meas}} - E_{\text{aoc}}$, where E_{meas} is the electrode potential (vs. SCE) of the same working electrode at which j_p is measured under irradiation and E_{aoc} is the electrode potential (vs. SCE) of the same working electrode under open circuit in the same electrolyte

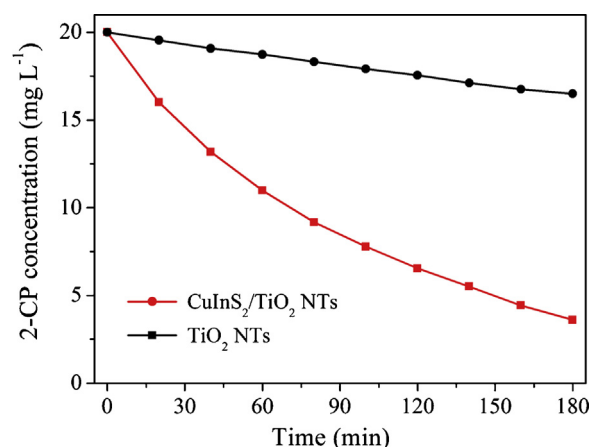


Fig. 13. The concentration vs. time plotted for photoelectron-catalytic degradation of 2-CP with TiO₂ NTs electrode, and CuInS₂/TiO₂ NTs electrode under visible light irradiation ($\lambda > 420$ nm, $I_0 = 35.5$ mW cm⁻², 0.6 V vs. SCE).

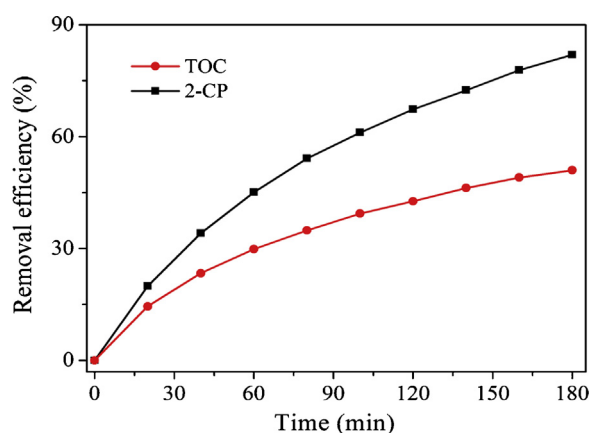


Fig. 14. Removal efficiency profiles of TOC and 2-CP during the PEC degradation for CuInS₂/TiO₂ NTs.

and under the same illumination. As shown in Fig. 12, the maximum photoconversion efficiency of 0.60% for the CuInS₂/TiO₂ NTs electrodes is observed at an applied potential of 0.40 V, while the pure TiO₂ NTs electrode has a maximum of 0.061%. The photoconversion efficiency improvement of the composite electrode indicates the photo-generated electrons are more efficiently injected from CuInS₂ to TiO₂ under the visible light irradiations.

The PEC activity of the CuInS₂/TiO₂ NTs electrode was measured by degradation of 2-CP under visible light irradiation ($\lambda > 420$ nm). For comparison, the pure TiO₂ NTs was investigated under the identical and parallel degradation conditions. As shown in Fig. 13, only 17.5% of 2-CP was degraded by the pure TiO₂ NTs electrode due to the adsorptive capacity of the porous structure. Additionally, the degradation efficiency of 2-CP was 81.95% with the CuInS₂/TiO₂ NTs electrode, suggesting that the PEC activity of the electrode was greatly enhanced by CuInS₂ modified. Fig. 14 depicts the removal efficiency of 2-CP and TOC in order to investigate the mineralization of 2-CP in the different times. During 180 min irradiation, the TOC was reduced continuously at a lower rate comparing with the PEC degradation of 2-CP. Only about 51% of 2-CP was mineralized. This difference indicated that some intermediate products were generated, which were not mineralized into CO₂ and H₂O in the degradation process, and complete mineralization of 2-CP needs more irradiation time.

In the subsequent PEC activity experiments, degradation of 2-CP with different processes under visible irradiation was

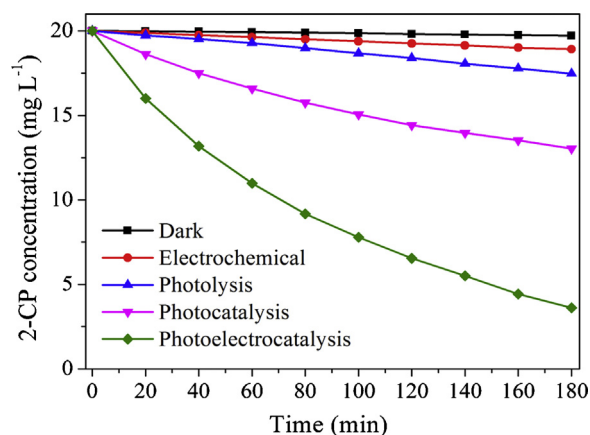


Fig. 15. The concentration vs. time plotted for degradation of 2-CP by different processes with $\text{CuInS}_2/\text{TiO}_2$ NTs electrode.

comparatively studied. As shown in Fig. 15, during degradation reaction, different processes exhibit discrepant PEC activities. Almost no 2-CP was reduced without light irradiation. The influence of 2-CP adsorption on the quartz reactor and the composite electrode could be ignored according to the adsorption test in dark upon the immersing of the electrode in the substrate solution. In addition, the direct photolysis process could remove 12.65% of 2-CP without any photocatalyst under visible light irradiations. Meanwhile, 5.4% of 2-CP was removed by direct electrochemical process with the bias potential of 0.6 V (vs. SCE), whereas 34.85% of 2-CP was decomposed by photocatalysis for the $\text{CuInS}_2/\text{TiO}_2$ NTs electrode. For the PEC process, the degradation efficiency eventually reached 81.95% for the $\text{CuInS}_2/\text{TiO}_2$ NTs electrode. It is obvious that the degradation efficiency of PEC process is more effective than the sum of the electrochemical and photocatalysis degradation process. These results further demonstrate that the $\text{CuInS}_2/\text{TiO}_2$ NTs electrode fabricated by ultrasonication-assisted electrodeposition have excellent PEC degradation efficiency of 2-CP upon visible light irradiations. Based on the above analysis, we would then conclude that the $\text{CuInS}_2/\text{TiO}_2$ NTs electrode has higher PEC performance and more impressive capacity and capability in organic pollutant degradation than TiO_2 NTs electrode.

3.1. Suggested photo-induced charge transfer mechanism

The photo-induced charge transfer mechanism for the $\text{CuInS}_2/\text{TiO}_2$ NTs heterostructure photoelectrode can be assumed in Fig. 16. As a narrow band gap semiconductor (1.5 eV), CuInS_2 could be easily excited by visible light irradiation and then the photoelectron from the valence band of CuInS_2 could transit to

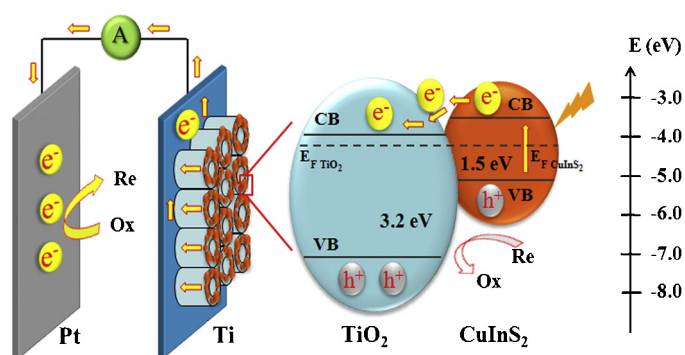


Fig. 16. Proposed photo-induced charge transfer process in the cell containing $\text{CuInS}_2/\text{TiO}_2$ NTs electrodes.

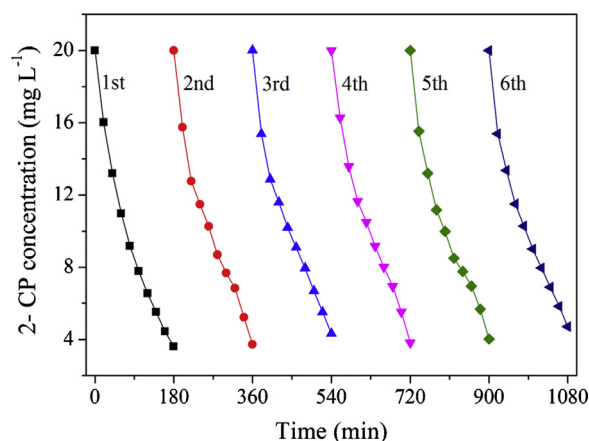


Fig. 17. Six repetitions for 2-CP PEC degradation with $\text{CuInS}_2/\text{TiO}_2$ NTs electrode under visible light irradiation (20 mg L^{-1} , $0.01 \text{ M Na}_2\text{SO}_4$, 0.6 V vs. SCE , $I_0 = 35.5 \text{ mW cm}^{-2}$).

the conduction band. When the n–n heterojunction between the n-type CuInS_2 and n-type TiO_2 has been formed, a thermodynamic equilibrium is achieved. Upon thermodynamic equilibrium, the two semiconductors have a uniform Fermi level [57]. With the same Fermi level, the energy level of conduction band edge for CuInS_2 is higher than that of TiO_2 . The electrons in CuInS_2 conduction band can be easily injected across the interface into the conduction band of TiO_2 , which serves as an electron transport medium. The accumulated photoelectrons in the conduction band of TiO_2 can transfer along the wall of TiO_2 nanotubes to the external circuit with the modulation of the external electrostatic field, and finally get to the counter electrode. On the other hand, the valence band holes of CuInS_2 could accumulate in the valence band to form hole centers. The holes accumulated both in TiO_2 and CuInS_2 can lead to the oxidation of 2-CP degradation. As a result, such n–n heterojunction of $\text{CuInS}_2/\text{TiO}_2$ NTs favors the electrons transfer, inhibits the recombination of photoelectrons and holes, and improves the photodegradation of 2-CP effectively.

In view of the further application, the stability of the modified electrode system is studied by repeating the PEC degradation of 2-CP under visible light irradiation. The experiment was carried out by introducing fresh 2-CP solution and Na_2SO_4 electrolyte for the PEC degradation of each new cycle. With the same irradiation time, the stability was determined from the cyclic curve. As shown in Fig. 17, after six cycles of PEC degradation, the degradation efficiency eventually attained to 76.50%, suggesting that $\text{CuInS}_2/\text{TiO}_2$ NTs electrode exhibited good stability. Coupled with the enhanced PEC activity, its potential application in PEC degradation of pollutants can be expected.

4. Conclusions

In summary, n-type CuInS_2 modified TiO_2 NTs heterojunction electrode has been successfully fabricated by an effective ultrasonication-assisted electrodeposition method. The characterization results show that CuInS_2 could effectively enhance the visible-light activity of TiO_2 NTs electrode and the n–n heterojunction structure could favor the surface-interface charge separation and transfer followed by dramatic suppression of the electron–hole recombination. The visible light PEC activity of $\text{CuInS}_2/\text{TiO}_2$ heterostructure photoelectrode was evaluated in degradation of 2-CP in aqueous solution, and it was indicated that the visible light photoelectrocatalytic activity of $\text{CuInS}_2/\text{TiO}_2$ NTs was improved significantly compared with the pure TiO_2 NTs. It is expected that such $\text{CuInS}_2/\text{TiO}_2$ NTs heterojunction electrode could be

promisingly employed for the photoelectrocatalytic degradation of various environmental pollutants utilizing solar energy.

Acknowledgements

This work was supported financially by the National Nature Science Foundation of China (21377015, 51178076), the Major State Basic Research Development Program of China (973 Program) (No. 2011CB936002) and the Key Laboratory of Industrial Ecology and Environmental Engineering, China Ministry of Education.

Appendix A. Supplementary data

Supplementary material related to this article can be found, in the online version, at <http://dx.doi.org/10.1016/j.apcatb.2014.03.035>.

References

- [1] V. Zwillling, E. Darque-Ceretti, A. Boutry-Forveille, D. David, M.Y. Perrin, M. Aucouturier, *Surf. Interface Anal.* 27 (1999) 629.
- [2] Y. Liu, B. Zhou, J. Bai, J. Li, J. Zhang, Q. Zheng, X. Zhu, W. Cai, *Appl. Catal. B: Environ.* 89 (2009) 142.
- [3] G.K. Mor, K. Shankar, M. Paulose, O.K. Varghese, C.A. Grimes, *Nano Lett.* 5 (2005) 191.
- [4] J.H. Park, S. Kim, A.J. Bard, *Nano Lett.* 6 (2006) 24.
- [5] G.K. Mor, K. Shankar, M. Paulose, O.K. Varghese, C.A. Grimes, *Nano Lett.* 6 (2006) 215.
- [6] K. Zhu, N.R. Neale, A. Miedaner, A.J. Frank, *Nano Lett.* 7 (2007) 69.
- [7] A. Lamberti, A. Sacco, S. Bianco, D. Manfredi, F. Cappelluti, S. Hernandez, D. Quaglio, C.F. Pirri, *Phys. Chem. Chem. Phys.* 15 (2013) 2596.
- [8] W. Sharmoukh, N.K. Allam, *ACS Appl. Mater. Interfaces* 4 (2012) 4413.
- [9] I.I.-D. Kim, A. Rothschild, B.H. Lee, D.Y. Kim, S.M. Jo, H.L. Tuller, *Nano Lett.* 6 (2006) 2009.
- [10] K. Shankar, G.K. Mor, A. Fitzgerald, C.A. Grimes, *J. Phys. Chem. C* 111 (2007) 21.
- [11] S. Yoriya, M. Paulose, O.K. Varghese, G.K. Mor, C.A. Grimes, *J. Phys. Chem. C* 111 (2007) 13770.
- [12] L. Sun, S. Zhang, X.W. Sun, X. Wang, Y. Cai, *Langmuir* 26 (2010) 18424.
- [13] A.G. Kontos, A. Katsanaki, V. Likodimos, T. Maggos, D. Kim, C. Vasilakos, D.D. Dionysios, P. Schmuki, P. Falaras, *Chem. Eng. J.* 179 (2012) 151.
- [14] Z.H. Zhang, Y. Yuan, G.Y. Shi, Y.J. Fang, L.H. Liang, H.C. Ding, L.T. Jin, *Environ. Sci. Technol.* 41 (2007) 6259.
- [15] Y. Hou, X.Y. Li, Q.D. Zhao, G.H. Chen, C.L. Raston, *Environ. Sci. Technol.* 46 (2012) 4042.
- [16] X.Y. Li, W. Teng, Q.D. Zhao, L.Z. Wang, *J. Nanopart. Res.* 13 (2011) 6813.
- [17] A.E.R. Mohamed, S. Rohani, *Energy Environ. Sci.* 4 (2011) 1065.
- [18] X.Y. Li, Y. Hou, Q.D. Zhao, W. Teng, X. Hu, G.H. Chen, *Chemosphere* 82 (2011) 581.
- [19] N. Lu, X. Quan, J.Y. Li, S. Chen, H.T. Yu, G.H. Chen, *J. Phys. Chem. C* 111 (2007) 11836.
- [20] I. Hanzu, T. Djenizian, G.F. Ortiz, P.J. Knauth, *J. Phys. Chem. C* 113 (2009) 20568.
- [21] Q. Li, J.K. Shang, *Environ. Sci. Technol.* 43 (2009) 8923.
- [22] C.J. Lin, Y.H. Yu, Y.H. Liou, *Appl. Catal. B: Environ.* 93 (2009) 119.
- [23] H.Y. Yang, S.F. Yu, S.P. Lau, X. Zhang, D.D. Sun, G. Jun, *Small* 5 (2009) 2260.
- [24] A. Furube, L.C. Du, K. Hara, R. Katoh, M. Tachiya, *J. Am. Chem. Soc.* 129 (2007) 14852.
- [25] J.P. Gueneau de Mussy, J.V. Macpherson, J.L. Delplancke, *Electrochim. Acta* 48 (2003) 1131.
- [26] W.T. Sun, Y. Yu, H.Y. Pan, X.F. Gao, Q. Chen, L.M. Peng, *J. Am. Chem. Soc.* 130 (2008) 1124.
- [27] A. Kongkanand, K. Tvrđy, K. Takechi, M. Kuno, P.V. Kamat, *J. Am. Chem. Soc.* 130 (2008) 4007.
- [28] R. Plass, S. Pelet, J. Krueger, M. Grätzel, *J. Phys. Chem. B* 106 (2002) 7578.
- [29] Q. Kang, S. Liu, L. Yang, Q. Cai, C.A. Grimes, *ACS Appl. Mater. Interfaces* 3 (2011) 746.
- [30] X. Sheng, L. Wang, L. Chang, Y. Luo, H. Zhang, J. Wang, D. Yang, *Chem. Commun.* 48 (2012) 4746.
- [31] M. Booth, A.P. Brown, S.D. Evans, K. Critchley, *Chem. Mater.* 24 (2012) 2064.
- [32] H.Z. Zhong, Y. Zhou, M.F. Ye, Y.J. He, J.P. Ye, C. He, C.H. Yang, Y.F. Li, *Chem. Mater.* 20 (2008) 6434.
- [33] M. Nanu, J. Schoonman, A. Goossens, *Adv. Mater.* 16 (2004) 453.
- [34] M. Nanu, J. Schoonman, A. Goossens, *Adv. Funct. Mater.* 15 (2005) 95.
- [35] R. O'Hayre, M. Nanu, J. Schoonman, A. Goossens, Q. Wang, M. Grätzel, *Adv. Funct. Mater.* 16 (2006) 1566.
- [36] J.H. Yun, Y.H. Ng, S. Huang, G. Conibeer, R. Amal, *Chem. Commun.* 47 (2011) 11288.
- [37] H.J. Lewerenz, *Sol. Energy Mater. Sol. Cells* 83 (2004) 395.
- [38] F.M. Courtel, R.W. Paynter, B. Marsan, M. Morin, *Chem. Mater.* 21 (2009) 3752.
- [39] X.F. Gao, W.T. Sun, Z.D. Hu, G. Ai, Y.L. Zhang, S. Feng, F. Li, L.M. Peng, *J. Phys. Chem. C* 113 (2009) 20481.
- [40] J. Llanosa, A. Buljan, C. Mujica, R. Ramírezb, J. Alloys Compd. 234 (1996) 40.
- [41] L.D. Partain, R.A. Schneider, L.F. Donaghey, P.S. McLeod, *J. Appl. Phys.* 57 (1985) 5056.
- [42] D.F. Hou, X.L. Hu, P. Hu, W. Zhang, M.F. Zhang, Y.H. Huang, *Nanoscale* 5 (2013) 9764.
- [43] J.F. Moulder, W.F. Stickle, P.E. Sobol, K.D. Bomben, *Handbook of X-ray Photoelectron Spectroscopy: A Reference Book of Standard Spectra for Identification and Interpretation of XPS Data*, Physical Electronic Division, Perkin-Elmer Corp., 1992.
- [44] Y. Hou, X.Y. Li, Q.D. Zhao, X. Quan, G.H. Chen, *Adv. Funct. Mater.* 20 (2010) 2165.
- [45] L.Q. Jing, X.J. Sun, J. Shang, W.M. Cai, Z.L. Xu, Y.G. Du, H.G. Fu, *Sol. Energy Mater. Sol. Cells* 79 (2003) 133.
- [46] Z.Y. Liu, D.D. Sun, P. Guo, J.O. Lechie, *Nano Lett.* 7 (2007) 1081.
- [47] L.Q. Jing, Y.C. Qu, B.Q. Wang, S.D. Li, B.J. Jiang, L.B. Yang, W. Fu, H.G. Fu, J.Z. Sun, *Sol. Energy Mater. Sol. Cells* 90 (2006) 1773.
- [48] T. Tachikawa, T. Majima, *Langmuir* 25 (2009) 7791.
- [49] J.G. Yu, H.G. Yu, B. Chen, X.J. Zhao, J.C. Yu, W.K. Ho, *J. Phys. Chem. B* 107 (2003) 13871.
- [50] X.Z. Li, F.B. Li, C.L. Yang, W.K. Ge, *J. Photochem. Photobiol. A* 141 (2001) 209.
- [51] F. Fabregat-Santiago, E.M. Barea, J. Bisquert, G.K. Mor, K. Shankar, C.A. Grimes, *J. Am. Chem. Soc.* 130 (2008) 11312.
- [52] J. Gong, W. Pu, C. Yang, J. Zhang, *Electrochim. Acta* 68 (2012) 178.
- [53] W. Teng, X.Y. Li, Q.D. Zhao, G.H. Chen, *J. Mater. Chem.* 1 (2013) 9060.
- [54] C. Baumanis, D.W. Bahnemann, *J. Phys. Chem. C* 112 (2008) 19097.
- [55] T. Gandhi, K.S. Raja, M. Misra, *Electrochim. Acta* 51 (2006) 5932.
- [56] Y. Hou, X.Y. Li, X.J. Zou, X. Quan, G.H. Zhen, *Environ. Sci. Technol.* 43 (2009) 858.
- [57] Y. Hu, D.Z. Li, Y. Zheng, W. Chen, Y.H. He, Y. Shao, X.Z. Fu, G.C. Xiao, *Appl. Catal. B: Environ.* 104 (2011) 30.